

RIS Assisted Device Activity Detection with Statistical Channel State Information

Friedemann Laue, *Graduate Student Member, IEEE*,

Vahid Jamali, *Member, IEEE*, and Robert Schober, *Fellow, IEEE*

Abstract

This paper studies reconfigurable intelligent surface (RIS) assisted device activity detection for grant-free (GF) uplink transmission in wireless communication networks. In particular, we consider mobile devices located in an area where the direct link to an access point (AP) is blocked. Thus, the devices try to connect to the AP via a reflected link provided by an RIS. Therefore, for the RIS, a phase-shift design is desired that covers the entire blocked area with a wide reflection beam because the exact locations and times of activity of the devices are unknown in GF transmission. In order to study the impact of the phase-shift design on the device activity detection at the AP, we derive a generalized likelihood ratio test (GLRT) based detector and present an analytical expression for the probability of detection, which is a function of the channel statistics and the phase-shift design. Assuming knowledge of statistical channel state information (CSI), we formulate an optimization problem for the phase-shift design for maximization of the guaranteed probability of detection for all locations within a given coverage area. To tackle the non-convexity of the problem, we propose two different approximations of the objective function and an algorithm based on the majorization-minimization (MM) principle. The first approximation leads to a design that aims to reduce the variations of the end-to-end channel while taking system parameters such as transmit power, noise power, and probability of false alarm into account. The second approximation can be adopted for versatile RIS deployments because it only depends on the line-of-sight (LoS) component of the end-to-end channel and is not affected by system parameters. For comparison, we also consider a phase-shift design maximizing the average channel

This work was presented in part at IEEE SPAWC 2021 [1]. (*Corresponding author: Friedemann Laue.*)

F. Laue and R. Schober are with Institute for Digital Communications, Friedrich-Alexander-Universität Erlangen-Nürnberg (FAU), 91058 Erlangen, Germany (e-mail: friedemann.laue@fau.de, robert.schober@fau.de).

F. Laue is also with Fraunhofer IIS, Fraunhofer Institute for Integrated Circuits IIS, Division Communication Systems (e-mail: friedemann.laue@iis.fraunhofer.de).

V. Jamali is with Department of Electrical Engineering and Information Technology, Technical University of Darmstadt, 64283 Darmstadt, Germany (e-mail: vahid.jamali@tu-darmstadt.de).

gain and a baseline analytical phase-shift design for large blocked areas. Our performance evaluation shows that the proposed approximations result in phase-shift designs that guarantee high probability of detection across the coverage area and outperform the baseline designs.

Index Terms

Device activity detection, reconfigurable intelligent surface, coverage extension, grant-free uplink, statistical channel state information, phase-shift design.

I. INTRODUCTION

Tunable metasurfaces that control the reflection properties of electromagnetic waves were proposed several years ago [2]. Recently, this technology has received significant attention in the wireless communications community. Its ability to create a smart radio environment helps in meeting the high performance requirements of future wireless networks [3]. To this end, metasurfaces are deployed as controllable passive reflectors, also known as reconfigurable intelligent surfaces (RISs). An RIS can be modelled as an array of small tunable elements, which are called *unit cells*. While an impinging electromagnetic wave is reflected on the surface of the RIS, the unit cells modify the characteristics of the wave, e.g., by applying individual phase shifts. Thereby, the configuration of the unit cells, or the *phase-shift design*, has an impact on the direction of reflection. The potential of this technology for practical deployments was demonstrated with first RIS prototypes. For example, indoor experiments with an RIS based on positive intrinsic-negative (PIN) diodes showed an antenna gain of up to 21.7 dBi [4]. Furthermore, an RIS employing varactor diodes and more than 1000 unit cells was successfully deployed to transmit a 1080p video stream, where a power consumption of only 1 W was observed [5].

A major challenge in the design of RIS assisted communication systems is the efficient computation of the phase shifts that maximize the desired system performance metric. One typical RIS use case are multi-user wireless communication networks, where an RIS is deployed to assist multiple users in performing uplink transmission to an access point (AP) [6]–[12]. For example, an optimization framework for maximization of both the energy efficiency and the spectral efficiency of RIS assisted multiple-input multiple-output (MIMO) uplink transmission was developed in [6]. This framework was used to provide optimized phase-shift designs while exploiting the instantaneous and statistical channel state information (CSI) of the cascaded RIS

channel. Moreover, power minimization in an RIS assisted multi-user multiple-input single-output (MISO) network was considered in [8]. After presenting a feasibility condition for a guaranteed information rate, an algorithm was developed that accounts for different quality of service (QoS) constraints for perfect and imperfect CSI. In addition, the rate performance of uplink MISO systems employing imperfect hardware was studied in [10] assuming perfect CSI. While impairments at both the AP and the RIS were considered, it was shown that the rate loss is mainly determined by the hardware limitations of the AP for typical numbers of RIS unit cells.

Whereas the above works assume scheduled uplink transmission and (imperfect) knowledge of the instantaneous CSI, in this paper, we focus on grant-free (GF) uplink transmission where the time of transmission is unknown at the AP. Consequently, device activity detection is required where only statistical CSI obtained from previous transmissions can be exploited.

GF transmission has been studied extensively in the literature and the main focus has recently been on device activity detection for massive connectivity [13]–[17]. For example, the authors of [13] analyzed compressed sensing techniques for device activity detection exploiting the sparse activity patterns in massive connectivity. It was shown that the probabilities of false alarm and missed detection asymptotically go to zero as the number of AP antennas goes to infinity. In addition, the authors of [14] proposed multi-user detection based on sparse user activity without the need for pilot signals in the context of massive connectivity. Furthermore, the authors of [15] developed an optimization framework for joint device activity detection and channel estimation, where the high complexity caused by large-scale antenna arrays and huge numbers of devices was made tractable by dimension reduction of the feasible space. Similarly, joint device activity detection and channel estimation was analyzed in [16]. More specifically, two compressed sensing based methods for joint multi-user detection and channel estimation in GF non-orthogonal multiple access systems were presented. Furthermore, the analysis of GF massive access was extended to multi-cell networks in [17]. In particular, device activities and interference powers were estimated using both cooperative and noncooperative approaches based on maximum likelihood and maximum a posteriori estimation.

Moreover, there is a small number of works that have investigated GF transmission and device activity detection in RIS assisted networks. For example, three recent studies focused on GF access for RIS assisted Internet of Things networks [18]–[20]. More specifically, assuming independent and identically distributed (i.i.d.) channel coefficients, sparse device activity, and

large RISs, the authors of [18] showed that the end-to-end channel can be characterized by a complex Gaussian distribution that is independent of the phase-shift design. This result was adopted to study channel estimation and device activity detection using a generalized approximate message passing algorithm. Similarly, the goal in [19] was to detect a set of active devices in a massive connectivity scenario and to estimate the RIS assisted channels. By exploiting the sparsity of both the channel and the device activity, an approximate message passing based algorithm for joint activity detection and channel estimation was developed assuming identical phase shifts for all unit cells. Furthermore, the authors of [20] focused on unsourced random access, which is an effective random access scheme for massive connectivity. In this context, joint user separation and channel estimation was supported by an RIS with a random phase-shift configuration.

As is evident from the above discussion, the phase shifts of the RISs in [18]–[20] were not specifically designed for the problem of device activity detection. However, the phase-shift design can have a significant impact on the detection performance in practical systems where signals propagate on a limited number of paths. In this case, it is important to apply a phase-shift design that takes the incident and reflected angles at the RIS into account [21]. Otherwise, device activity detection at the AP may fail because the devices' locations are not covered by the RIS reflection pattern [22].

To this end, the authors of the recent work [23] proposed a random access protocol that sweeps through a finite set of RIS configurations. In particular, a downlink phase and an uplink phase are used to estimate the channel and to connect to the AP, respectively. Although this protocol significantly improves the access performance, the model in [23] assumes a simplified setup with line-of-sight (LoS) links and one-dimensional phase-shift configurations. In addition, the protocol causes access delays due to the training phase, and device activity detection at the AP was not considered in [23].

In this paper, we study RIS phase-shift design for GF access and device activity detection, and extend the analysis of our previous work [1]. In particular, we consider a communication system where the direct link from the AP to a pre-defined area is blocked. Thus, an RIS is deployed to connect the AP with mobile devices located in the blocked area through a reflected link. In contrast to [18]–[20], [23], in this paper, we optimize the phase-shift design to maximize the minimum probability of detection for any device within the blocked area. Intuitively, since the devices' exact locations and times of transmission are unknown for GF access, the challenge is

to develop a phase-shift design that covers the entire area with a wide reflection beam.

To this end, we propose a generalized likelihood ratio test (GLRT) based detector and formulate an optimization problem that maximizes the probability of detection across all locations within the blocked area. Since the optimization problem is non-convex and involves the Marcum Q function, we reformulate the problem considering two approximations of the Marcum Q function and solve it applying the majorization-minimization (MM) principle, where each approximation results in a different phase-shift design. Finally, we adopt the proposed GLRT detector to evaluate the detection performance of these designs. For comparison, we consider an alternative design approach that maximizes the average channel gain and a baseline analytical design.

The main contributions of this paper can be summarized as follows:

- We investigate device activity detection for RIS assisted communication systems using a geometric channel model based on statistical CSI. Our analysis includes both the LoS and non-line-of-sight (NLoS) paths of the device-RIS channels and takes into account their incident and reflected angles at the RIS. To this end, we adopt a physics-based RIS model for characterization of the angle-dependent reflection gain.
- Based on the GLRT, we derive a device activity detector and analyze its performance. In particular, we show that the probability of detection can be expressed in terms of the Marcum Q function and it depends on the phase-shift design of the RIS and the statistics of the channel.
- We formulate the phase-shift design as an optimization problem for maximization of the minimum probability of detection across all locations within a given coverage area. In order to tackle the non-convexity of the problem, we propose two approximations for the objective function and reformulate them as differences-of-convex (DC) functions. This allows us to solve the problem exploiting the MM principle and obtain a high-quality suboptimal phase-shift design for each approximation.
- We evaluate the detection performance for the proposed design approach and show that our method outperforms existing schemes for RIS phase-shift design. In particular, the proposed design approach improves the probability of device activity detection compared to a design maximizing the average channel gain [24]–[26] and an analytical phase-shift design for large coverage areas [1], [27].

Different from its conference version [1], this paper takes both the LoS and NLoS paths of the device-RIS channels into account. As a result, the detection performance cannot be expressed as

a monotonic function of the LoS channel gain as in [1], i.e., a different approach for phase-shift design is required. Similar to [1], the design proposed in this work is based on a non-convex optimization problem. However, instead of resolving the non-convexity of the problem using semidefinite relaxation and Gaussian randomization, we rewrite the non-convex terms in DC form and apply the MM principle. In addition, we investigate the impact of different transmit powers, scattering strengths, incident angles at the RIS, and area sizes. We also study the reflection patterns of the optimized phase-shift designs.

The remainder of this paper is organized as follows. Section II introduces the system and channel models. The GLRT for the considered device activity detection problem is derived in Section III. We formulate the optimization problem for the phase-shift design in Section IV, and present the MM based solution in Section V. The performance of the proposed phase-shift designs is evaluated in Section VI, and conclusions are drawn in Section VII.

Notations: $\text{Tr}(\cdot)$, $(\cdot)^T$, $(\cdot)^H$, $(\cdot)^{-1}$, and $\mathbb{E}[\cdot]$ denote the trace, transpose, conjugate transpose, inverse, and expectation operations, respectively. $\|\cdot\|$ refers to the Euclidean norm of a vector and $|\cdot|$ represents the absolute value of a scalar. The nuclear norm and spectral norm of a matrix are denoted by $\|\cdot\|_*$ and $\|\cdot\|_2$, respectively. Given a function $f(\mathbf{X})$ with matrix argument \mathbf{X} , $\nabla_{\mathbf{X}}f$ represents the gradient of $f(\mathbf{X})$. The element in the m th row and n th column of a matrix and the n th element of a vector are denoted by $[\cdot]_{m \times n}$ and $[\cdot]_n$, respectively. The determinant of matrix \mathbf{X} is denoted by $\det(\mathbf{X})$, the identity matrix is denoted by \mathbf{I} , and a positive semidefinite matrix \mathbf{X} is denoted by $\mathbf{X} \succeq 0$. \mathbb{R} and \mathbb{C} represent the sets of real and complex numbers, respectively. $\mathbf{x} \sim \mathcal{CN}(\mathbf{a}, \mathbf{B})$ refers to a complex normally distributed random vector \mathbf{x} with mean vector \mathbf{a} and covariance matrix \mathbf{B} . $\chi_a^2(b)$ represents a noncentral chi-squared distribution with a degrees of freedom and noncentrality parameter b . Probability is denoted by $\Pr\{\cdot\}$. The operator $\lfloor x \rfloor$ represents the largest integer less than or equal to x and the remainder of the division a/b is denoted by $a \pmod{b}$. The exponential function $e^{(\cdot)}$ is also written as $\exp(\cdot)$.

II. SYSTEM MODEL

In this section, we present the considered communication network, where the direct link from the AP to a specific area is blocked. As illustrated in Fig. 1, mobile devices located within the blocked area connect to the AP via the reflected link of the RIS. In the following, we introduce the coordinate system for the communication network and describe the coverage area, the RIS, and the AP in more detail. Additionally, we present the adopted channel model.

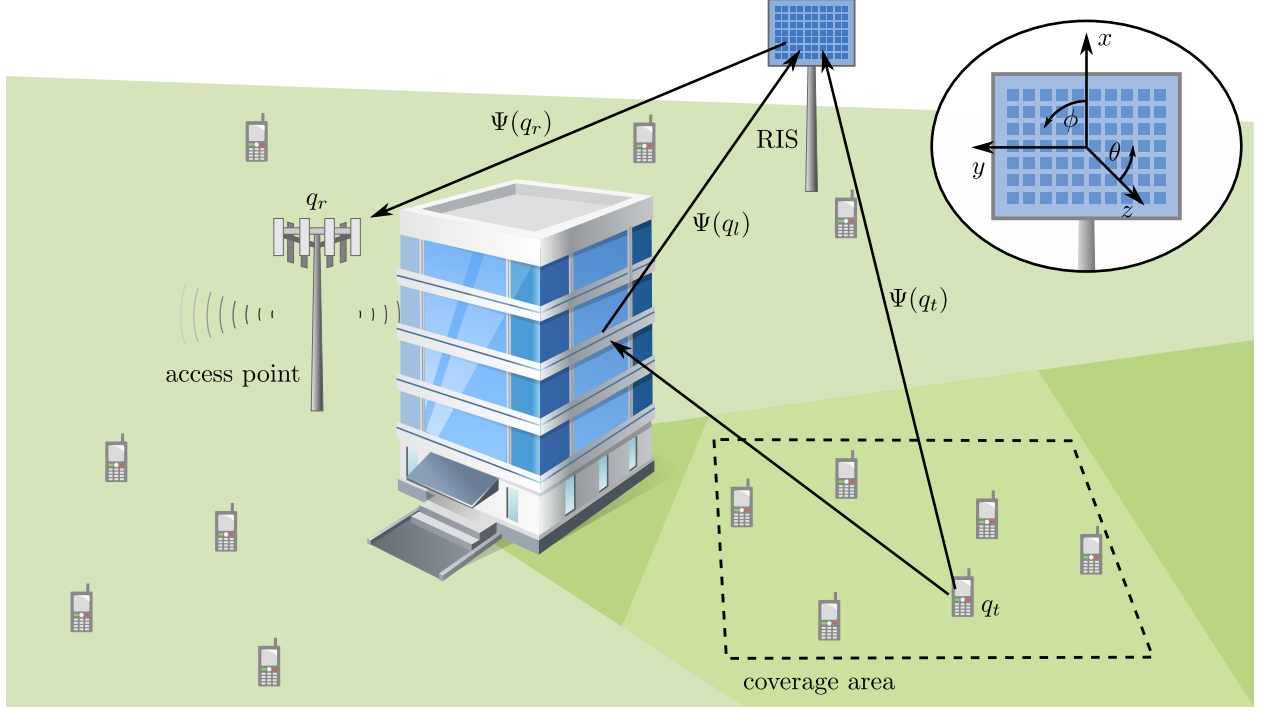


Fig. 1: Illustration of the considered communication setup for device activity detection.

A. Coordinate System

We place the origin of the coordinate system at the center of the RIS and refer to a location in three-dimensional space as q . Location q is specified by Cartesian coordinates $\text{cart}(q) = (x_q, y_q, z_q)$ or spherical coordinates $\text{sph}(q) = (d_q, \theta_q, \phi_q)$, where d_q , θ_q , and ϕ_q denote the distance from the origin to q , the elevation angle of q , and the azimuth angle of q , respectively. Further, we denote the direction from the origin to location q as $\Psi(q) = (\theta_q, \phi_q)$.

B. Coverage Area and Transmitters

The actual coverage area is an arbitrary area in continuous three-dimensional space, e.g., an area in the y - z plane. For tractability, we take Q samples of the continuous area and define the approximated coverage area as the discrete set of locations $\mathcal{Q} = \{q_{t,1}, q_{t,2}, \dots, q_{t,Q}\}$. The number of samples can be chosen according to the desired approximation accuracy [1]. For simplicity, we assume a rectangular coverage area with center coordinates (c_x, c_y, c_z) , length D_z in z -direction, and width D_y in y -direction.

The location of a device is denoted as q_t , where $q_t \in \mathcal{Q}$ holds for devices located within the coverage area. We consider single-antenna devices that try to connect to the AP by transmitting

a preamble sequence, which is defined by symbol vector $\mathbf{s} \in \mathbb{C}^S$ of length S . We assume normalized symbols, i.e., $|\mathbf{s}_s|^2 = 1, \forall s \in \{1, \dots, S\}$.

C. Access Point

We consider an M -antenna AP deployed at a fixed and known location q_r . Furthermore, we assume a linear receiver with coherent combining and a LoS link¹ to the RIS. Thus, the AP can be modelled as an equivalent single-antenna receiver with beamforming gain M . The transmitted signal of an active device is received via the RIS at the AP as²

$$\mathbf{x} = h\sqrt{MP_{\text{tx}}}\mathbf{s} + \mathbf{n}, \quad (1)$$

where $h \in \mathbb{C}$, $P_{\text{tx}} \in \mathbb{R}$, and $\mathbf{n} \in \mathbb{C}^S$ denote the end-to-end channel gain, the transmit power, and additive Gaussian noise, respectively. The noise is modelled as $\mathbf{n} \sim \mathcal{CN}(\mathbf{0}, \sigma^2 \mathbf{I})$ with noise power σ^2 . Note that h depends on the phase-shift design and the channel model, which is presented in Section II-E.

D. Reconfigurable Intelligent Surface

It has been shown that the reflection gain of the RIS depends on the angles of arrival (AoAs) and angles of departure (AoDs) of the incident and reflected waves, respectively [5], [21], [30]. Therefore, in order to correctly model the reflection gain for the different device locations, we adopt the physics-based RIS model from [21]. In particular, we assume that the RIS is centered at the origin of the coordinate system and is modelled as a uniform planar array (UPA) with $U_x U_y = U$ unit cells in the x - y plane. The location of unit cell $u \in \{0, 1, \dots, U - 1\}$ is given by the coordinate vector

$$\mathbf{c}_u = \begin{bmatrix} d_x u_x & d_y u_y & 0 \end{bmatrix}^T, \quad (2)$$

¹In RIS assisted networks, it is usually desired that the RIS is deployed with dominant LoS to the AP in order to achieve the maximum received power [28], [29]. Thus, similar to [23]–[25], [28], [29], we assume that in the AP-RIS channel the impact of fading is negligible and consider only the LoS path.

²For the phase-shift design of the RIS, we assume that only one device is active at a time. However, the phase-shift designs proposed in this paper provide wide reflection beams that cover a given area, i.e., these designs extend the coverage of the AP. Thus, the designs can be straightforwardly combined with existing schemes for multi-user detection, channel estimation, and data transmission designed for non-RIS assisted multi-user networks.

where d_x and d_y denote the unit cell spacing along the x and y axis, respectively, and

$$u_x = u \pmod{U_x} - U_x/2 + 1 \quad (3)$$

$$u_y = \lfloor u/U_x \rfloor - U_y/2 + 1. \quad (4)$$

Here, we assume that U_x and U_y are even numbers. The response function of the RIS is given by [21]

$$g(\Psi(q_r), \Psi(q_t)) = \frac{\sqrt{4\pi}}{\lambda} c(\Psi(q_r), \Psi(q_t)) \mathbf{w}^H \mathbf{a}(\Psi(q_r), \Psi(q_t)), \quad (5)$$

where $\lambda \in \mathbb{R}$, $c(\Psi(q_r), \Psi(q_t)) \in \mathbb{C}$, $\mathbf{w} \in \mathbb{C}^U$, and $\mathbf{a}(\Psi(q_r), \Psi(q_t)) \in \mathbb{C}^U$ denote the wavelength, the unit cell factor, the phase-shift vector, and the array response, respectively. Defining

$$\mathbf{k}(\Psi(q)) = \frac{2\pi}{\lambda} \begin{bmatrix} \sin(\theta_q) \cos(\phi_q) & \sin(\theta_q) \sin(\phi_q) & \cos(\theta_q) \end{bmatrix}^T \quad (6)$$

and $\mathbf{k}(q_r, q_t) = \mathbf{k}(\Psi(q_r)) + \mathbf{k}(\Psi(q_t))$, the array response can be expressed as

$$\mathbf{a}(\Psi(q_r), \Psi(q_t)) = \begin{bmatrix} e^{j\mathbf{k}^T(q_r, q_t)\mathbf{c}_0} & e^{j\mathbf{k}^T(q_r, q_t)\mathbf{c}_1} & \dots & e^{j\mathbf{k}^T(q_r, q_t)\mathbf{c}_{U-1}} \end{bmatrix}^T. \quad (7)$$

The u th element of \mathbf{w} is given by $e^{j\omega_u}$, where ω_u denotes the phase shift applied by the u th unit cell. Unit cell factor $c(\Psi(q_r), \Psi(q_t))$ describes the amplitude of the reflection coefficient of each unit cell, which depends on the incident and reflected angles, the polarization of the incident wave, and the physical realization of the unit cells. For example, using the physics-based model of [21], the unit cell factor is given by

$$c(\Psi(q_r), \Psi(q_t)) = \frac{j\sqrt{4\pi}d_xd_y}{\lambda} \times \cos(\theta_{q_t}) \frac{\left\| \begin{bmatrix} \cos(\varphi_{q_t}) \cos(\theta_{q_r}) \sin(\phi_{q_r}) - \sin(\varphi_{q_t}) \cos(\theta_{q_r}) \cos(\phi_{q_r}) \\ \sin(\varphi_{q_t}) \sin(\phi_{q_r}) + \cos(\varphi_{q_t}) \cos(\phi_{q_r}) \end{bmatrix} \right\|_2}{\sqrt{(\cos(\varphi_{q_t}) \sin(\theta_{q_t}) \cos(\phi_{q_t}) + \sin(\varphi_{q_t}) \sin(\theta_{q_t}) \sin(\phi_{q_t}))^2 + \cos^2(\theta_{q_t})}}, \quad (8)$$

where φ_{q_t} denotes the polarization of the incident wave originating from location q_t .

E. Channel Model

We assume that the direct link between the coverage area and the AP is blocked, cf. Fig. 1. Therefore, the devices have to connect with the AP via the reflected link, which comprises the device-RIS and the RIS-AP links. As stated in Section II-C, the RIS-AP link is dominated by the LoS path. For the device-RIS link, the scattered paths cannot be neglected because the devices

are located close to the ground [31], [32]. Nevertheless, we assume a limited number of clusters of scatterers [21]. Furthermore, the clusters' incident directions at the RIS are fixed and equal for all locations within the coverage area [31]. Therefore, the channel in (1) can be modelled as follows

$$h = \bar{h}(q_r) \left(\bar{h}(q_t)g(\Psi(q_r), \Psi(q_t)) + \sum_{l=1}^L \eta_l(q_t)g(\Psi(q_r), \Psi(q_l)) \right), \quad (9)$$

where L , $\Psi(q_l)$, and $\eta_l(q_t) \sim \mathcal{CN}(0, \sigma_l^2(q_t))$ denote the number of clusters, the incident direction of the l th cluster on the RIS, and the small-scale fading with variance $\sigma_l^2(q_t)$ caused by the l th cluster, respectively, and $\bar{h}(q)$ denotes the LoS channel coefficient between the RIS and location q . Note that the variances of the small-scale fading may change for different device locations, i.e., variance $\sigma_l^2(q_t)$ depends on q_t . Also, similar to [19], [20], [33], [34], we assume narrow-band communication, i.e., the delays between different propagation paths are not resolvable. The channel gain $\bar{h}(q)$ can be written as $\bar{h}(q) = |\bar{h}(q)|e^{j\varphi(q)}$, where magnitude $|\bar{h}(q)| = \lambda/(4\pi d_q)$ is given by the free-space path loss and depends on wavelength λ and distance d_q between location q and the RIS. The phase shift $\varphi(q) = 2\pi d_q/\lambda$ depends on the wavelength and the distance as well.

Remark 1. In the following, we assume that $\Psi(q_l)$ and $\sigma_l^2(q_t), \forall l \in \{1, \dots, L\}$, are known based on channel measurements for previous transmissions [35].

Remark 2. We note that, in practice, the accuracy of the (measured) distance d_q is limited and may not be in the order of the wavelength. As a result, we assume that the phase terms $e^{j\varphi(q_r)}$ and $e^{j\varphi(q_t)}$ are unknown [1]. In contrast, small deviations of d_q do not have a significant impact on the channel magnitude. Thus, we assume that $|\bar{h}(q)|$ is known.

Substituting (5) in (9) allows us to rewrite the channel coefficient as follows

$$h = \mathbf{w}^H (\mathbf{h}^{\text{LoS}} + \mathbf{h}^{\text{NLoS}}), \quad (10)$$

where

$$\mathbf{h}^{\text{LoS}} = \frac{\sqrt{4\pi}}{\lambda} \bar{h}(q_r) \bar{h}(q_t) c(\Psi(q_r), \Psi(q_t)) \mathbf{a}(\Psi(q_r), \Psi(q_t)) \quad (11a)$$

$$\mathbf{h}^{\text{NLoS}} = \frac{\sqrt{4\pi}}{\lambda} \bar{h}(q_r) \sum_{l=1}^L \eta_l c(\Psi(q_r), \Psi(q_l)) \mathbf{a}(\Psi(q_r), \Psi(q_l)). \quad (11b)$$

Based on (10), we note that phase-shift vector \mathbf{w} has an impact on the end-to-end channel h . Moreover, we conclude that h can be modelled as a complex Gaussian random variable with $h \sim \mathcal{CN}(\mathbf{w}^H \mathbf{h}^{\text{LoS}}, \mathbf{w}^H \mathbf{C} \mathbf{w})$, where

$$\mathbf{C} = \frac{4\pi}{\lambda^2} |\bar{h}(q_r)|^2 \sum_{l=1}^L \sigma_l^2(q_t) |c(\Psi(q_r), \Psi(q_l))|^2 \mathbf{a}(\Psi(q_r), \Psi(q_l)) \mathbf{a}^H(\Psi(q_r), \Psi(q_l)). \quad (12)$$

III. DEVICE ACTIVITY DETECTION

In this section, we consider the problem of device activity detection and derive analytical expressions for the detection performance. In general, for a given desired probability of false alarm, the maximum probability of detection of an active device is obtained with the likelihood ratio test (LRT) [36]. However, the LRT requires full knowledge of the distribution of the end-to-end channel. We observe from (11) and (12) that the variance of the channel is known, but the mean value depends on the unknown phase terms of the LoS paths, cf. Remark 2. Therefore, we use estimates of the unknown terms for the derivation of the detector, which results in a GLRT [36].

For derivation of the proposed detector, we exploit the following lemma.

Lemma 1. For $\mathbf{x}, \mathbf{y} \in \mathbb{C}^N$, $z, \gamma \in \mathbb{C}$, $c_1, c_2 \in \mathbb{R} \setminus \{0\}$, and $\mathbf{C} = c_1 \mathbf{y} \mathbf{y}^H + c_2 \mathbf{I}$, the following identity holds:

$$\min_{\gamma} (\mathbf{x} - \mathbf{y} z \gamma)^H \mathbf{C}^{-1} (\mathbf{x} - \mathbf{y} z \gamma) = (\mathbf{x} - \frac{1}{\mathbf{y}^H \mathbf{y}} \mathbf{y} \mathbf{y}^H \mathbf{x})^H \mathbf{C}^{-1} (\mathbf{x} - \frac{1}{\mathbf{y}^H \mathbf{y}} \mathbf{y} \mathbf{y}^H \mathbf{x}). \quad (13)$$

Proof. Given $\mathbf{H} \in \mathbb{C}^{N \times p}$ and $\mathbf{C} \in \mathbb{C}^{N \times N}$, let $\mathbf{x} \sim \mathcal{CN}(\mathbf{H} \boldsymbol{\theta}, \mathbf{C})$ with the unknown vector $\boldsymbol{\theta} \in \mathbb{C}^p$. Then, the maximum likelihood estimate (MLE) of $\boldsymbol{\theta}$ is given by [37, Chapter 15]

$$\hat{\boldsymbol{\theta}} = (\mathbf{H}^H \mathbf{C}^{-1} \mathbf{H})^{-1} \mathbf{H}^H \mathbf{C}^{-1} \mathbf{x}. \quad (14)$$

The left-hand side of (13) is equivalent to finding the MLE of γ for $\mathbf{x} \sim \mathcal{CN}(\mathbf{y} z \gamma, \mathbf{C})$. Hence, with $\mathbf{H} = \mathbf{y} z$ and $\boldsymbol{\theta} = \gamma$, we obtain the MLE

$$\hat{\gamma} = \frac{1}{z} \frac{\mathbf{y}^H \mathbf{C}^{-1} \mathbf{x}}{\mathbf{y}^H \mathbf{C}^{-1} \mathbf{y}}. \quad (15)$$

The inverse of $\mathbf{C} = c_1 \mathbf{y} \mathbf{y}^H + c_2 \mathbf{I}$ is found with the Woodbury matrix identity (matrix inversion lemma) as

$$\mathbf{C}^{-1} = \frac{1}{c_2} \left(\mathbf{I} - \frac{c_1 \mathbf{y} \mathbf{y}^H}{c_2 + c_1 \mathbf{y}^H \mathbf{y}} \right). \quad (16)$$

Substituting (16) in (15) results in

$$\hat{\gamma} = \frac{1}{z} \frac{\mathbf{y}^H \mathbf{x}}{\mathbf{y}^H \mathbf{y}}, \quad (17)$$

which gives the value for γ that minimizes the left-hand side of (13). The right-hand side is obtained by substituting (17) for γ in (13). \square

A. Detection Problem

Device activity detection at the AP can be described as a binary hypothesis test problem [36]. More specifically, we define hypothesis \mathcal{H}_0 for an inactive device and hypothesis \mathcal{H}_1 for an active device. Hence, received signal \mathbf{x} can be written as

$$\mathcal{H}_0 : \mathbf{x} = \mathbf{n} \quad (18a)$$

$$\mathcal{H}_1 : \mathbf{x} = h\sqrt{P}\bar{\mathbf{s}} + \mathbf{n}, \quad (18b)$$

where (18a) contains noise only and (18b) follows from (1) with $P = MP_{\text{tx}}S$ and $\bar{\mathbf{s}} = \sqrt{\frac{1}{S}}\mathbf{s}$. Here, we normalize \mathbf{s} to obtain $\|\bar{\mathbf{s}}\|^2 = 1$, which simplifies the derivations in the following sections. Using the channel model in (10), we obtain

$$\mathcal{H}_0 : \mathbf{x} \sim \mathcal{CN}(0, \mathbf{C}_0) \quad (19a)$$

$$\mathcal{H}_1 : \mathbf{x} \sim \mathcal{CN}(\boldsymbol{\mu}(\gamma), \mathbf{C}_1), \quad (19b)$$

where

$$\gamma = e^{j(\varphi(q_r) + \varphi(q_t))} \quad (20)$$

$$\boldsymbol{\mu}(\gamma) = \mathbf{w}^H \frac{\sqrt{4\pi}}{\lambda} |\bar{h}(q_r)| |\bar{h}(q_t)| \gamma c(\Psi(q_r), \Psi(q_t)) \mathbf{a}(\Psi(q_r), \Psi(q_t)) \sqrt{P}\bar{\mathbf{s}} \quad (21)$$

$$\mathbf{C}_0 = \sigma^2 \mathbf{I} \quad (22)$$

$$\mathbf{C}_1 = \mathbf{w}^H \mathbf{C} \mathbf{w} P \bar{\mathbf{s}} \bar{\mathbf{s}}^H + \sigma^2 \mathbf{I}. \quad (23)$$

In (20) and (21), we introduce parameter γ comprising the phase terms of the LoS links, which constitutes the unknown parameter for the GLRT.

B. Detection Metric

In general, the GLRT of a binary hypothesis test problem is based on a detection metric $T(\mathbf{x})$ that is derived from the likelihood ratio of both hypotheses. This metric is compared to a threshold t and the detector assumes that \mathcal{H}_1 is the true hypothesis when $T(\mathbf{x}) > t$ holds for received signal \mathbf{x} [36].

For the problem at hand, the log-likelihood ratio for the hypotheses in (18) is given by [36]

$$L_G(\mathbf{x}, \gamma) = \log \left(\frac{\det(\mathbf{C}_0) \exp \left(-(\mathbf{x} - \boldsymbol{\mu}(\gamma))^H \mathbf{C}_1^{-1} (\mathbf{x} - \boldsymbol{\mu}(\gamma)) \right)}{\det(\mathbf{C}_1) \exp \left(-\mathbf{x}^H \mathbf{C}_0^{-1} \mathbf{x} \right)} \right). \quad (24)$$

The dependence on unknown parameter γ is resolved by finding the best estimate $\hat{\gamma}$ for detection, i.e., finding $\hat{\gamma}$ that maximizes (24) [36]. Using Lemma 1, we obtain

$$\max_{\gamma} L_G(\mathbf{x}, \gamma) = \log \left(\frac{\det(\mathbf{C}_0) \exp \left(-(\mathbf{x} - \bar{\mathbf{s}}\bar{\mathbf{s}}^H \mathbf{x})^H \mathbf{C}_1^{-1} (\mathbf{x} - \bar{\mathbf{s}}\bar{\mathbf{s}}^H \mathbf{x}) \right)}{\det(\mathbf{C}_1) \exp \left(-\mathbf{x}^H \mathbf{C}_0^{-1} \mathbf{x} \right)} \right) \quad (25a)$$

$$= \log \left(\frac{\det(\mathbf{C}_0)}{\det(\mathbf{C}_1)} \right) + \mathbf{x}^H \mathbf{C}_0^{-1} \mathbf{x} - (\mathbf{x} - \bar{\mathbf{s}}\bar{\mathbf{s}}^H \mathbf{x})^H \mathbf{C}_1^{-1} (\mathbf{x} - \bar{\mathbf{s}}\bar{\mathbf{s}}^H \mathbf{x}). \quad (25b)$$

The first term in (25b) is independent of \mathbf{x} and can be neglected for detection. Thus, the detection metric of the GLRT is given by

$$T(\mathbf{x}) = \mathbf{x}^H \mathbf{C}_0^{-1} \mathbf{x} - (\mathbf{x} - \bar{\mathbf{s}}\bar{\mathbf{s}}^H \mathbf{x})^H \mathbf{C}_1^{-1} (\mathbf{x} - \bar{\mathbf{s}}\bar{\mathbf{s}}^H \mathbf{x}) \quad (26a)$$

$$= \mathbf{x}^H (\mathbf{C}_0^{-1} - \mathbf{C}_1^{-1}) \mathbf{x} - \mathbf{x}^H \bar{\mathbf{s}}\bar{\mathbf{s}}^H \mathbf{C}_1^{-1} \bar{\mathbf{s}}\bar{\mathbf{s}}^H \mathbf{x} + \mathbf{x}^H \mathbf{C}_1^{-1} \bar{\mathbf{s}}\bar{\mathbf{s}}^H \mathbf{x} + \mathbf{x}^H \bar{\mathbf{s}}\bar{\mathbf{s}}^H \mathbf{C}_1^{-1} \mathbf{x}. \quad (26b)$$

Since $\mathbf{C}_0^{-1} = \sigma^{-2} \mathbf{I}$ and \mathbf{C}_1^{-1} is found with (16) and (23), (26) simplifies to

$$T(\mathbf{x}) = \frac{1}{\sigma^2} |\bar{\mathbf{s}}^H \mathbf{x}|^2, \quad (27)$$

which is a correlation detector for the known preamble sequence $\bar{\mathbf{s}}$.

C. Detection Performance

In order to determine the performance of detection metric (27), we examine the distribution of $T(\mathbf{x})$. Based on (18) and (19), (27) can be written as

$$\mathcal{H}_0 : T(\mathbf{x}) = \frac{1}{\sigma^2} |\bar{\mathbf{s}}^H \mathbf{n}|^2 = \frac{1}{2} z_0 \quad (28a)$$

$$\mathcal{H}_1 : T(\mathbf{x}) = \frac{1}{\sigma^2} \left| \bar{\mathbf{s}}^H \left(h\sqrt{P}\bar{\mathbf{s}} + \mathbf{n} \right) \right|^2 = \frac{\mathbf{w}^H \mathbf{C} \mathbf{w} P + \sigma^2}{2\sigma^2} z_1, \quad (28b)$$

where

$$z_0 = \frac{2}{\sigma^2} |\bar{\mathbf{s}}^H \mathbf{n}|^2 \sim \chi_2^2(0) \quad (29a)$$

$$z_1 = \frac{2}{\mathbf{w}^H \mathbf{C} \mathbf{w} P + \sigma^2} \left| \bar{\mathbf{s}}^H \left(h\sqrt{P}\bar{\mathbf{s}} + \mathbf{n} \right) \right|^2 \sim \chi_2^2 \left(2P \frac{|\mathbf{w}^H \mathbf{h}^{\text{LoS}}|^2}{\mathbf{w}^H \mathbf{C} \mathbf{w} P + \sigma^2} \right). \quad (29b)$$

Thus, in general, the detection metric follows a scaled noncentral chi-squared distribution, where both the scaling factor and the noncentrality parameter take different values under \mathcal{H}_0 and \mathcal{H}_1 .

The noncentrality parameter under \mathcal{H}_0 equals zero, i.e., the probability of false alarm is given by

$$P_F = \Pr \left\{ \frac{1}{2} z_0 > t \right\} = 1 - (1 - e^{-t}). \quad (30)$$

Thus, for a desired P_F , the detection threshold is obtained as $t = -\ln(P_F)$. The probability of detection is then given by

$$P_D = \Pr \left\{ \frac{\mathbf{w}^H \mathbf{C} \mathbf{w} P + \sigma^2}{2\sigma^2} z_1 > t \right\} = \Pr \left\{ z_1 > \frac{-2\sigma^2 \ln(P_F)}{\mathbf{w}^H \mathbf{C} \mathbf{w} P + \sigma^2} \right\}. \quad (31)$$

Since z_1 is a noncentral chi-squared random variable, (31) can be expressed as follows

$$P_D = Q_1 \left(\sqrt{2P \frac{|\mathbf{w}^H \mathbf{h}^{\text{LoS}}|^2}{\mathbf{w}^H \mathbf{C} \mathbf{w} P + \sigma^2}}, \sqrt{\frac{-2\sigma^2 \ln(P_F)}{\mathbf{w}^H \mathbf{C} \mathbf{w} P + \sigma^2}} \right), \quad (32)$$

where $Q_1(a, b) = \int_b^\infty t e^{-\frac{t^2+a^2}{2}} I_0(at) dt$ denotes the first-order Marcum Q function for $b \geq 0$, $a > 0$, and $I_0(\cdot)$ denotes the modified Bessel function of the first kind of order 0 [38].

Remark 3. The probability of detection in (32) depends on both the mean value and the variance of the end-to-end channel. If the variance is zero, i.e., the channel comprises the LoS path only, the second parameter of Q_1 in (32) becomes independent of \mathbf{w} . Then, P_D simplifies to the expression in [1, Eq. (19)], where the scattered paths of the device-RIS channels were not taken into account.

IV. PHASE-SHIFT DESIGN

In this section, we first formulate a non-convex optimization problem to obtain the optimal phase-shift design for device activity detection. In order to tackle the non-convexity, we reformulate the problem and propose two approximations of the objective function, each leading to a different suboptimal phase-shift design. The reformulated problem is solved with an algorithm exploiting the MM principle. Moreover, we investigate the maximization of the average channel gain as an alternative phase-shift design criterion.

A. Optimal Phase-Shift Design

Recall that the RIS is deployed to assist the detection of devices that try to connect to the AP, where the exact locations of the devices are not known. Therefore, we aim for a phase-shift design that maximizes the guaranteed detection performance, i.e., the minimum probability of

detection for any device location within the coverage area. Thus, the optimal phase-shift design is obtained based on

$$\max_{\mathbf{w} \in \mathbb{C}^U} \min_{q_t \in \mathcal{Q}} Q_1 \left(\sqrt{2P \frac{|\mathbf{w}^H \mathbf{h}^{\text{LoS}}|^2}{\mathbf{w}^H \mathbf{C} \mathbf{w} P + \sigma^2}}, \sqrt{\frac{-2\sigma^2 \ln(P_F)}{\mathbf{w}^H \mathbf{C} \mathbf{w} P + \sigma^2}} \right) \quad (33a)$$

$$\text{s.t. } |[\mathbf{w}]_u| = 1, \forall u \in \{0, \dots, U-1\}. \quad (33b)$$

Optimization problem (33) cannot be solved directly because both constraint (33b) and the Marcum Q function are non-convex. Although the studies in [39], [40] showed that $Q_1(a, b)$ is monotonic and log-concave with respect to either a or b , these results only hold when the other parameter is fixed. Thus, they are not applicable to (33) because both parameters a and b depend on optimization variable \mathbf{w} .

Moreover, tight bounds and alternative representations of $Q_1(a, b)$ were proposed in [41] and [42], respectively, which provide simplified analytical expressions of the Marcum Q function. However, these results do not lead to a tractable form for the optimization problem in (33).

Therefore, we propose two approximations of the Marcum Q function that facilitate solving (33). We denote the resulting approximate objective functions, which will be derived in Sections IV-C and IV-D, respectively, as $J_k(\mathbf{W}, q_t)$, $k \in \{1, 2\}$, where $\mathbf{W} = \mathbf{w}\mathbf{w}^H \in \mathbb{C}^{U \times U}$ and $q_t \in \mathcal{Q}$ denote optimization variables.

B. Reformulation to Min-Max SDP

Let $J_k(\mathbf{W}, q_t)$ denote an approximation of the negative³ Marcum Q function in (33), where $\mathbf{W} = \mathbf{w}\mathbf{w}^H$. Then, (33) can be written as follows

$$\min_{\mathbf{W} \in \mathbb{C}^{U \times U}} \max_{q_t \in \mathcal{Q}} J_k(\mathbf{W}, q_t) \quad (34a)$$

$$\text{s.t. } \mathbf{W} \succeq 0 \quad (34b)$$

$$[\mathbf{W}]_{u \times u} = 1, \forall u \in \{0, \dots, U-1\} \quad (34c)$$

$$\text{rank}(\mathbf{W}) = 1, \quad (34d)$$

which is the well-known semidefinite programming (SDP) representation of a min-max optimization problem with a unit-modulus optimization variable. Constraint (34d) guarantees that the optimal vector \mathbf{w} can be obtained from the decomposition of \mathbf{W} and (34c) ensures that the

³Note the change of objective from max-min to min-max in (34).

elements of \mathbf{w} have unit magnitude. Note that problem (34) is still non-convex due to constraint (34d), but we will show in Section V that this constraint can be replaced by adding a convex penalty term to the objective function.

C. Lower Bound

As a first approximation, we adopt a lower bound of $Q_1(a, b)$, which maintains the general goal of the desired phase-shift design, i.e., maximizing a guaranteed probability of detection. It has been shown that [39], [43]

$$Q(b+a) + Q(b-a) = Q_{0.5}(a, b) < Q_1(a, b) \quad (35)$$

for $a \geq 0$ and $b > 0$, where $Q(x) = \frac{1}{\sqrt{2\pi}} \int_x^\infty e^{-\frac{t^2}{2}} dt$ denotes the Gaussian Q-function. Since $0 \leq Q(b+a) \leq Q(b-a)$ holds, we neglect $Q(b+a)$ in (35) and define the lower bound

$$Q(b-a) < Q_1(a, b), \quad (36)$$

where

$$a = \sqrt{2P \frac{\text{Tr}(\mathbf{W}\mathbf{M})}{\text{Tr}(\mathbf{W}\mathbf{C})P + \sigma^2}} \quad (37)$$

$$b = \sqrt{\frac{-2\sigma^2 \ln(P_F)}{\text{Tr}(\mathbf{W}\mathbf{C})P + \sigma^2}} \quad (38)$$

are found from (32) with $\mathbf{M} = \mathbf{h}^{\text{LoS}} (\mathbf{h}^{\text{LoS}})^H$. Note that (36) is tight⁴ if the LoS component of the channel is dominant compared to the NLoS component, because $Q(b-a) \approx Q_1(a, b)$ for $b \gg 1$ and $b \gg b-a$ [38]. The probability of detection is maximized when the argument $b-a$ in (36) is minimized, leading to objective function

$$\tilde{J}_1(\mathbf{W}, q_t) = \frac{\sqrt{-2\sigma^2 \ln(P_F)} - \sqrt{2P \text{Tr}(\mathbf{W}\mathbf{M})}}{\sqrt{\text{Tr}(\mathbf{W}\mathbf{C})P + \sigma^2}}. \quad (39)$$

The fraction is avoided with the equivalent objective function

$$J_1(\mathbf{W}, q_t) = \ln \left(\sqrt{\text{Tr}(\mathbf{W}\mathbf{C})P + \sigma^2} \right) - \ln \left(\sqrt{2P \text{Tr}(\mathbf{W}\mathbf{M})} - \sqrt{-2\sigma^2 \ln(P_F)} \right), \quad (40)$$

which is used in (34) to obtain the optimal phase-shift vector for the lower-bound approximation of (32).

⁴The accuracies of the bounds in (35) and (36) are discussed in Section VI-C.

From (40) we observe that minimizing $J_1(\mathbf{W}, q_t)$ implies minimizing the contribution of the NLoS component and maximizing the contribution of the LoS component, which are reflected in the first and second term of (40), respectively. In addition, we note that solving (34) with $J_1(\mathbf{W}, q_t)$ as objective function results in a phase-shift vector that depends on the noise power, the transmit power, the probability of false alarm, and the channel statistics.

D. Objective Function for Strong LoS Path

The advantage of objective function (40) is that both the system parameters and the channel statistics are taken into account, which leads to phase-shift designs that accurately match a specific scenario. However, in practice, phase-shift designs that are applicable for different parameter sets may be preferable. For example, a design approach that is independent of the device's transmit power allows a more versatile deployment of the RIS.

This can be accomplished by neglecting the scattered paths of the channel, which is a reasonable approximation for channels with a strong LoS component⁵. Thus, by assuming $\text{Tr}(\mathbf{W}\mathbf{C}) \approx 0$, $J_1(\mathbf{W}, q_t)$ becomes a monotonic function in $\text{Tr}(\mathbf{W}\mathbf{M})$, which allows us to define the equivalent objective function

$$J_2(\mathbf{W}, q_t) = -\text{Tr}(\mathbf{W}\mathbf{M}). \quad (41)$$

Similarly, it is straightforward to verify that P_D in (32) is monotonic in $|\mathbf{w}^H \mathbf{h}^{\text{LoS}}|^2$ if $\mathbf{w}^H \mathbf{C} \mathbf{w} \approx 0$. Objective function (41) only depends on the LoS component of the channel and is not affected by the transmit power, the noise power, and the desired probability of false alarm. We note that $J_2(\mathbf{W}, q_t)$ has been used as objective function in the conference version of this paper [1, Eq. (20)], cf. Remark 3.

E. Average Channel Gain

For RIS phase-shift design, besides the maximization of the probability of detection, the maximization of the average channel gain seems to be a desirable objective [24]–[26]. The average channel gain is given by $\mathbb{E}[|h|^2] = |\mathbf{w}^H \mathbf{h}^{\text{LoS}}|^2 + \mathbf{w}^H \mathbf{C} \mathbf{w} = \text{Tr}(\mathbf{W}(\mathbf{M} + \mathbf{C}))$, which can be maximized for all locations $q_t \in \mathcal{Q}$ using objective function⁶

$$J_3(\mathbf{W}, q_t) = -\text{Tr}(\mathbf{W}(\mathbf{M} + \mathbf{C})) \quad (42)$$

⁵The impact of neglecting the scattered paths is evaluated in Section VI-C.

⁶One can find an upper bound of P_D based on Markov's inequality, given by $P_D \leq (\text{Tr}(\mathbf{W}(\mathbf{M} + \mathbf{C}))P + \sigma^2)/(-\sigma^2 \ln(P_F))$. Interestingly, maximizing this bound is equivalent to minimizing $J_3(\mathbf{W}, q_t)$.

in (34). We consider $J_3(\mathbf{W}, q_t)$ for the performance evaluation in Section VI and compare it to the results obtained with $J_1(\mathbf{W}, q_t)$ and $J_2(\mathbf{W}, q_t)$. Similar to $J_2(\mathbf{W}, q_t)$, $J_3(\mathbf{W}, q_t)$ does not depend on the transmit power, noise power, and probability of false alarm. In contrast, $J_3(\mathbf{W}, q_t)$ is only affected by the statistics of the channel.

V. OPTIMIZATION ALGORITHM

In the previous section, three objective functions for the min-max SDP in (34) were proposed. However, problem (34) cannot be solved directly because (34d) is a non-convex constraint. Therefore, we reformulate (34) in this section and exploit the MM principle to obtain a suboptimal phase-shift design for each objective function.

A. Problem Reformulation

Problem (34) can be equivalently rewritten as

$$\min_{\mathbf{W} \in \mathbb{C}^{U \times U}, m \in \mathbb{R}} m + \rho (\|\mathbf{W}\|_* - \|\mathbf{W}\|_2) \quad (43a)$$

$$\text{s.t. } \mathbf{W} \succeq 0 \quad (43b)$$

$$[\mathbf{W}]_{u \times u} = 1, \forall u \in \{0, \dots, U-1\} \quad (43c)$$

$$J_k(\mathbf{W}, q_t) \leq m, \forall q_t \in \mathcal{Q}, \quad (43d)$$

where the max operation in (34a) is replaced by constraint (43d) and rank-one constraint (34d) is rewritten as a penalty term in (43a). More specifically, exploiting $\|\mathbf{W}\|_* - \|\mathbf{W}\|_2 = 0 \Leftrightarrow \text{rank}(\mathbf{W}) = 1$, it has been shown that the solution of (43) is rank one if penalty factor $\rho > 0$ is sufficiently large [44].

In order to obtain optimized phase-shift designs based on (43), we examine the convexity of (43) for $k \in \{1, 2, 3\}$. We note that $J_2(\mathbf{W}, q_t)$ and $J_3(\mathbf{W}, q_t)$ are convex functions, and that $J_1(\mathbf{W}, q_t)$ and the objective function in (43a) are in DC form. Thus, (43) can be solved using the MM principle, i.e., we apply convex upper bounds to the DC terms and iteratively solve the resulting optimization problem until convergence [45]. The upper bounds are found as follows.

Lemma 2. Let $f(\mathbf{W}) = f_{\text{cvx}}(\mathbf{W}) + f_{\text{ccv}}(\mathbf{W})$ denote a function in DC form, i.e., $f_{\text{cvx}}(\mathbf{W})$ and $f_{\text{ccv}}(\mathbf{W})$ denote a convex and a concave function in $\mathbf{W} \succeq 0$, respectively. Then, $f(\mathbf{W})$ is bounded as

$$f(\mathbf{W}) \leq \bar{f}(\mathbf{W}) = f_{\text{cvx}}(\mathbf{W}) + \bar{f}_{\text{ccv}}(\mathbf{W}), \quad (44)$$

where $\bar{f}(\mathbf{W})$ is a convex function in \mathbf{W} and

$$\bar{f}_{\text{ccv}}(\mathbf{W}) = f_{\text{ccv}}(\mathbf{W}') + \text{Tr}(\nabla_{\mathbf{W}}^H f_{\text{ccv}}(\mathbf{W}') (\mathbf{W} - \mathbf{W}')) \quad (45)$$

denotes the first-order approximation of $f_{\text{ccv}}(\mathbf{W})$ at $\mathbf{W}' \succeq 0$.

Proof. Since $f_{\text{ccv}}(\mathbf{W})$ is a concave function and \mathbf{W}, \mathbf{W}' are from a convex set, the first-order approximation of $f_{\text{ccv}}(\mathbf{W})$ at \mathbf{W}' is a global overestimator of $f_{\text{ccv}}(\mathbf{W})$, i.e., $f_{\text{ccv}}(\mathbf{W}) \leq \bar{f}_{\text{ccv}}(\mathbf{W})$ [46]. Adding $f_{\text{cvx}}(\mathbf{W})$ to this inequality results in (44). \square

Corollary 1. Given $\mathbf{W}' \succeq 0$, a convex upper bound of the objective function in (43a) is given by

$$m + \rho \text{Tr}\left(\left(\mathbf{I} - \mathbf{v}' \mathbf{v}'^H\right) \mathbf{W}\right) - \rho \|\mathbf{W}'\|_2 + \rho \text{Tr}\left(\mathbf{v}' \mathbf{v}'^H \mathbf{W}'\right), \quad (46)$$

where \mathbf{v}' denotes the eigenvector that corresponds to the largest eigenvalue of \mathbf{W}' .

Proof. Using Lemma 2, we find

$$\|\mathbf{W}\|_* - \|\mathbf{W}\|_2 \leq \|\mathbf{W}\|_* - \|\mathbf{W}'\|_2 - \text{Tr}(\mathbf{v}' \mathbf{v}'^H (\mathbf{W} - \mathbf{W}')) \quad (47)$$

because $\nabla_{\mathbf{W}} \|\mathbf{W}'\|_2 = \mathbf{v}' \mathbf{v}'^H$ [34], [47]. Using the identity $\|\cdot\|_* = \text{Tr}(\cdot)$ for positive semidefinite matrices and substituting the bound in (47) into (43a) results in (46). \square

Corollary 2. Given $\mathbf{W}' \succeq 0$, objective function $J_1(\mathbf{W}, q_t)$ is bounded as

$$\begin{aligned} J_1(\mathbf{W}, q_t) \leq \bar{J}_1(\mathbf{W}, \mathbf{W}', q_t) = & -\ln\left(\sqrt{2P\text{Tr}(\mathbf{W}\mathbf{M})} - \sqrt{-2\sigma^2 \ln(P_F)}\right) \\ & + \ln\left(\sqrt{\text{Tr}(\mathbf{W}'\mathbf{C})P + \sigma^2}\right) + \frac{1}{2} \frac{\text{Tr}(\mathbf{C}(\mathbf{W} - \mathbf{W}'))P}{\text{Tr}(\mathbf{W}'\mathbf{C})P + \sigma^2} \end{aligned} \quad (48)$$

Proof. Objective function $J_1(\mathbf{W}, q_t)$ can be written as

$$J_1(\mathbf{W}, q_t) = J_{1,\text{cvx}}(\mathbf{W}, q_t) + J_{1,\text{ccv}}(\mathbf{W}, q_t), \quad (49)$$

where

$$J_{1,\text{cvx}}(\mathbf{W}, q_t) = -\ln\left(\sqrt{2P\text{Tr}(\mathbf{W}\mathbf{M})} - \sqrt{-2\sigma^2 \ln(P_F)}\right) \quad (50)$$

$$J_{1,\text{ccv}}(\mathbf{W}, q_t) = \ln\left(\sqrt{\text{Tr}(\mathbf{W}\mathbf{C})P + \sigma^2}\right) \quad (51)$$

denote a convex and a concave function, respectively. The gradient of $J_{1,\text{ccv}}(\mathbf{W}, q_t)$ is given by

$$\nabla_{\mathbf{W}} J_{1,\text{ccv}}(\mathbf{W}, q) = \frac{1}{2} \frac{\mathbf{C}P}{\text{Tr}(\mathbf{W}\mathbf{C})P + \sigma^2}, \quad (52)$$

Algorithm 1: Phase-Shift Optimization

```

Define  $\mathcal{Q}$ ,  $k$ ,  $\rho$ ,  $\nu$ , and  $\mathbf{w}_0$ ;
 $i \leftarrow 0$ ;
 $\mathbf{W}_i, \mathbf{v}_i, \Omega_i \leftarrow \mathbf{w}_i \mathbf{w}_i^H, \mathbf{w}_i, \max_{q_t \in \mathcal{Q}} J_k(\mathbf{W}_i, q_t)$ ;
repeat
     $\mathbf{W}', \mathbf{v}' \leftarrow \mathbf{W}_i, \mathbf{v}_i$ ;
     $\mathbf{W}_{i+1}, m_{i+1} \leftarrow \text{solve}(\text{problem (53)})$ ;
     $\mathbf{v}_{i+1} \leftarrow \text{decompose}(\mathbf{W}_{i+1})$ ;
     $\Omega_{i+1} \leftarrow \max_{q_t \in \mathcal{Q}} J_k(\mathbf{W}_{i+1}, q_t)$ ;
     $i \leftarrow i + 1$ ;
until  $\left| \frac{\Omega_i - \Omega_{i-1}}{\Omega_{i-1}} \right| \leq \nu$ ;
 $\mathbf{w}_{\text{opt}} \leftarrow \mathbf{v}_i$ ;
  
```

which is found by applying the chain rule while taking the derivate of $J_{1,\text{ccv}}(\mathbf{W}, q)$ with respect to \mathbf{W} . Then, (48) follows from Lemma 2. \square

Now, we use Corollary 1 to replace the objective function in (43a) with its upper bound. In addition, we replace $J_k(\mathbf{W}, q_t)$ with $\bar{J}_k(\mathbf{W}, \mathbf{W}', q_t)$, where $\bar{J}_1(\mathbf{W}, \mathbf{W}', q_t)$ is given in Corollary 2, $\bar{J}_2(\mathbf{W}, \mathbf{W}', q_t) = J_2(\mathbf{W}, q_t)$, and $\bar{J}_3(\mathbf{W}, \mathbf{W}', q_t) = J_3(\mathbf{W}, q_t)$. The resulting convex optimization problem for $k \in \{1, 2, 3\}$ is given as follows

$$\min_{\mathbf{W} \in \mathbb{C}^{U \times U}, m \in \mathbb{R}} m + \rho \text{Tr} \left(\left(\mathbf{I} - \mathbf{v}' \mathbf{v}'^H \right) \mathbf{W} \right) \quad (53a)$$

$$\text{s.t. } \mathbf{W} \succeq 0 \quad (53b)$$

$$[\mathbf{W}]_{u \times u} = 1, \forall u \in \{0, \dots, U-1\} \quad (53c)$$

$$\bar{J}_k(\mathbf{W}, \mathbf{W}', q_t) \leq m, \forall q_t \in \mathcal{Q}, \quad (53d)$$

where (53a) is obtained from (46) neglecting the terms not depending on \mathbf{W} or m .

Then, according to the MM principle, problem (53) is iteratively solved as follows. Given a feasible point $\mathbf{W}_i = \mathbf{w}_i \mathbf{w}_i^H$ for the i th iteration of the algorithm, we set $\mathbf{v}' = \mathbf{w}_i$ and $\mathbf{W}' = \mathbf{W}_i$, and denote the solution of (53) as \mathbf{W}_{i+1} . As summarized in Algorithm 1, these steps are repeated until the objective function converges, i.e., the relative difference between the optimal values Ω_i and Ω_{i-1} is smaller than threshold ν .

B. Convergence and Computational Complexity

Algorithm 1 follows the MM principle and iteratively solves (53), which tightens the upper bound of (43) in each iteration. Thus, the sequence $\{\mathbf{W}_i, m_i\}_{i \in \mathbb{N}}$ provides non-increasing sequences of objective values for (43) and for its equivalent formulation (34). Furthermore, these objective values converge to a stationary value because the objective functions of (43) and (34) are bounded below. As a result, the limit point of the sequence $\{\mathbf{W}_i, m_i\}_{i \in \mathbb{N}}$ obtained with Algorithm 1 converges to a stationary point of problem (34) [45].

The computational complexity of Algorithm 1 mainly depends on the complexity of convex optimization problem (53). For a given solution accuracy of $\epsilon > 0$, problem (53) can be numerically solved with a worst-case complexity of $\mathcal{O}\left((Q + U)^4 \sqrt{U} \log\left(\frac{1}{\epsilon}\right)\right)$ [48]. As one can see, the complexity polynomially depends on the number of unit cells and the number of considered device locations. However, since (53) does not depend on instantaneous CSI, the problem does not have to be solved in an online manner.

VI. PERFORMANCE EVALUATION

In this section, we evaluate the detection performance for different system parameters and compare the results obtained with objective functions $J_1(\mathbf{W}, q_t)$, $J_2(\mathbf{W}, q_t)$, and $J_3(\mathbf{W}, q_t)$. More specifically, we apply Algorithm 1 for $k \in \{1, 2, 3\}$, which results in three optimized phase-shift vectors $\mathbf{w}_{\text{opt},1}$, $\mathbf{w}_{\text{opt},2}$, and $\mathbf{w}_{\text{opt},3}$. Then, for each phase-shift vector, we use (32) to evaluate the minimum probability of detection across all locations within the coverage area, i.e., we plot $\min_{q_t \in \mathcal{Q}} P_D(q_t)$. For convenience, we omit the arguments (\mathbf{W}, q_t) for the following discussion.

A. Baseline Phase-Shift Design

We also compare the performance of our proposed phase-shift designs with the quadratic phase-shift design in [1], [27], which is an analytical phase-shift design for large coverage areas. In addition, this design is used for initialization of \mathbf{w}_0 in Algorithm 1. Therefore, our evaluation will reveal the performance gain achieved by the additional effort of iteratively solving optimization problem (53).

B. System and Channel Parameters

The system parameters for the performance evaluation are summarized in Table I. Furthermore, since a suitable value of penalty factor ρ depends on k , P_{tx} , K , etc., we select ρ based on the

TABLE I: System parameters.

Parameter	Value	Parameter	Value	Parameter	Value	Parameter	Value
(c_x, c_y, c_z)	$(-10 \text{ m}, -30 \text{ m}, 30 \text{ m})$	(U_x, U_y)	$(4, 8)$	M	4	φ_{q_t}	0°
$d_{q_r}, \Psi(q_r)$	$25 \text{ m}, (90^\circ, 37^\circ)$	(d_x, d_y)	$(\lambda/2, \lambda/2)$	S	64	P_F	0.1
D_z	20 m	λ	0.1 m	σ^2	-100 dBm	ν	10^{-7}

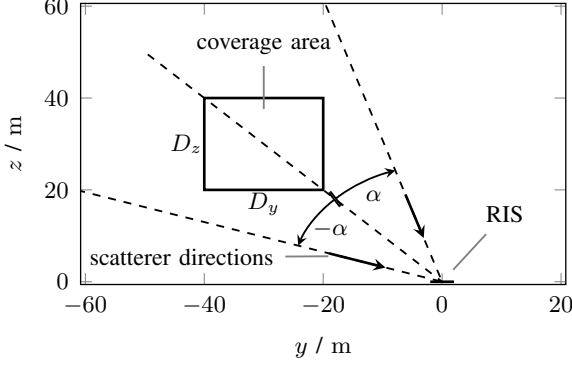
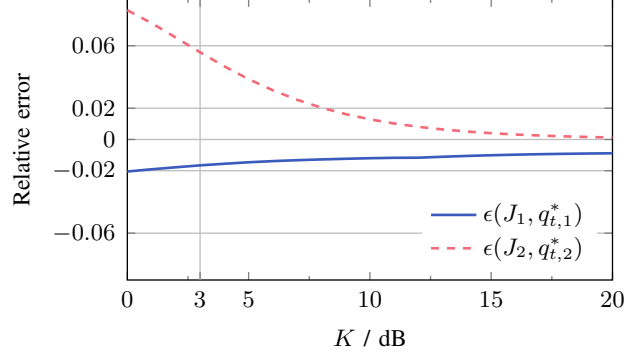


Fig. 2: Schematic top view of the scenario.

Fig. 3: Relative error of approximations for J_1 and J_2 as a function of K .

set $\{1, 10, 100, 1000\}$ for each considered case. Moreover, we study different channel conditions of the device-RIS link by varying the power ratio of the LoS and NLoS components, given by $K = |\bar{h}(q_t)|^2 / \sum_{l=1}^L \sigma_l^2(q_t)$. For simplicity, we assume equal variances $\bar{\sigma}^2(q_t) = \sigma_l^2(q_t), \forall l \in \{1, \dots, L\}$, for all scattered paths, which results in $\bar{\sigma}^2(q_t) = |\bar{h}(q_t)|^2 / (KL)$. Furthermore, we assume $L = 2$ scattered paths and characterize their incident directions with angle α as shown in Fig. 2.

C. Accuracy of Approximation

First, we examine the accuracy of lower bound (36) that results in objective function J_1 . In addition, we quantify the effect of neglecting the scattered paths, which is used to arrive at objective function J_2 . To this end, let a_k and b_k denote parameters a in (37) and b in (38), respectively, evaluated for $\mathbf{W}_k = \mathbf{w}_{\text{opt},k} \mathbf{w}_{\text{opt},k}^H$, $k \in \{1, 2\}$. Furthermore, we define $\tilde{a}_k = a_k|_{\text{Tr}(\mathbf{W}_k \mathbf{C})=0}$ and $\tilde{b}_k = b_k|_{\text{Tr}(\mathbf{W}_k \mathbf{C})=0}$, respectively, which represent a_k and b_k when the scattered paths are neglected. Then, $Q(b_1 - a_1)$ is the lower bound for $Q_1(a_1, b_1)$ that leads to J_1 and $Q_1(\tilde{a}_2, \tilde{b}_2)$ is the approximation of $Q_1(a_2, b_2)$ that results in J_2 . Thus, the relative errors for J_1 and J_2 at location q_t are given by $\epsilon(J_1, q_t) = Q(b_1 - a_1) / Q_1(a_1, b_1) - 1$ and

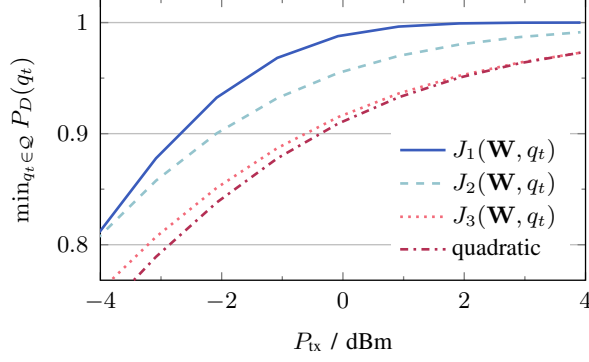


Fig. 4: Minimum probability of detection as a function of the transmit power for $K = 3$ dB, $\alpha = 30^\circ$, and $D_y = 20$ m.

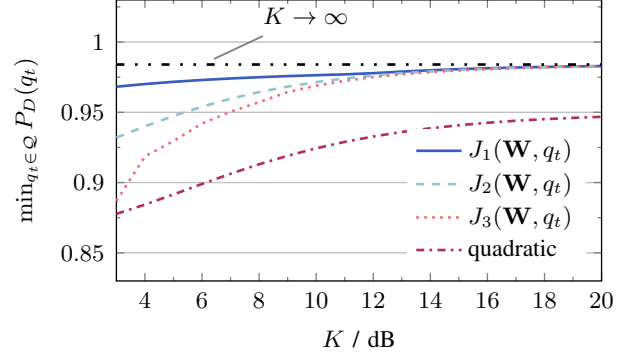


Fig. 5: Minimum probability of detection as a function of K for $D_y = 20$ m, $P_{tx} = -1$ dBm, and $\alpha = 30^\circ$.

$\epsilon(J_2, q_t) = Q_1(\tilde{a}_2, \tilde{b}_2)/Q_1(a_2, b_2) - 1$, respectively. The largest relative errors across the coverage area for J_1 and J_2 are observed at $q_{t,1}^* = \arg \max_{q_t \in \mathcal{Q}} |Q(b_1 - a_1) - Q_1(a_1, b_1)|/Q_1(a_1, b_1)$ and $q_{t,2}^* = \arg \max_{q_t \in \mathcal{Q}} |Q_1(\tilde{a}_2, \tilde{b}_2) - Q_1(a_2, b_2)|/Q_1(a_2, b_2)$, respectively.

For the system parameters described in Section VI-B and Table I, Fig. 3 shows $\epsilon(J_1, q_{t,1}^*)$ and $\epsilon(J_2, q_{t,2}^*)$ for different values of K , where we set $D_y = 20$ m, $P_{tx} = -1$ dBm, and $\alpha = 30^\circ$. One can see that the relative error for J_1 remains below 0.02 for all K . Furthermore, we observe that the relative error for J_2 approaches zero for large K , but increases for low K . However, for the performance evaluation, we consider RIS deployments that result in channels with a dominant LoS component [49], [50]. Thus, assuming $K \geq 3$ dB, Fig. 3 confirms that J_1 and J_2 are accurate approximations with relative errors smaller than 0.06.

D. Impact of Transmit Power

The dependence of the detection performance on the transmit power is shown in Fig. 4. As expected, we observe an improvement of the detection performance for all phase-shift designs as the transmit power increases. Furthermore, for high transmit powers, the minimum probability of detection across the coverage area approaches 1 in all cases. In addition, Fig. 4 indicates that phase shifts designed based on J_1 and J_2 outperform those designed based on J_3 and the baseline quadratic design. The best performance is achieved with J_1 , which improves the detection performance of the baseline quadratic design from 0.91 to 0.99 for $P_{tx} = 0$ dBm.

The differences in performance among the optimized phase-shift designs can be explained considering the different objective functions. More specifically, the detection performance in

Fig. 4 depends on both the transmit power and the reflection gain of the RIS. For J_2 and J_3 , the reflection gains are constant for all values of P_{tx} because both objective functions are independent of the transmit power. In contrast, the phase-shift design obtained for J_1 adapts to P_{tx} , i.e., the reflection beam can be made narrower as the transmit power increases, which yields a better performance. Moreover, J_2 yields better results than J_3 . Both objective functions maximize the power of the LoS paths but J_3 also enhances the power of the scattered paths, which leads to more variations in the effective end-to-end channel and worse detection performance.

E. Impact of Scattering Strength

The relation between the LoS and the NLoS components in the channel also plays an important role for phase-shift optimization, which is illustrated in Fig. 5. One can see that the detection performance increases with the value of K and that all optimized phase-shift designs converge for $K \rightarrow \infty$ to the asymptotic performance of 0.984. This behavior can be explained with the reduced variations in the channel as K increases. For $K \rightarrow \infty$, $\mathbf{w}^H \mathbf{C} \mathbf{w} \rightarrow 0$ and the channel becomes fully deterministic. In this case, J_1 , J_2 , and J_3 are equivalent.

For small values of K , similar to Fig. 4, J_1 achieves the highest probability of detection, followed by J_2 , J_3 , and the baseline quadratic design.

F. Impact of Scattering Directions

In addition to the scattering strength, the incident directions of the scattered paths have an impact on the detection performance, too. In order to evaluate this dependence in more detail, Fig. 6 depicts the probability of detection for $\alpha \in \{10^\circ, 20^\circ, 30^\circ\}$, which corresponds to scattering within the coverage area, near the edge of the coverage area, and with large distance to the coverage area, respectively, see Fig. 2. Interestingly, J_2 provides the best performance for $\alpha = 10^\circ$, but J_1 is superior for $\alpha \in \{20^\circ, 30^\circ\}$. This observation can be explained as follows.

Recall that J_1 is minimized by maximizing the power of the LoS paths and minimizing the power of the NLoS paths, which can be done concurrently and independently if both channel components are separable in the angular domain. For $\alpha \in \{20^\circ, 30^\circ\}$, the separation is possible because the scattering is outside the coverage area. In this case, objective function J_1 results in a phase-shift design that suppresses the scattered paths, and thus achieves the best detection performance.

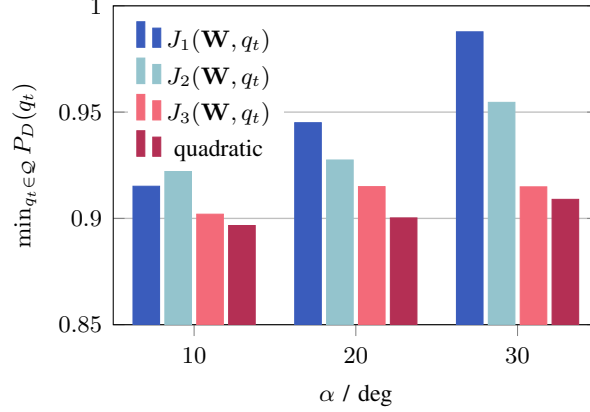


Fig. 6: Minimum probability of detection for $\alpha \in \{10^\circ, 20^\circ, 30^\circ\}$, $D_y = 20$ m, $P_{\text{tx}} = 0$ dBm, and $K = 3$ dB.

However, separation is not possible for $\alpha = 10^\circ$. Consequently, there is a design conflict for J_1 because minimizing the power of the scattered paths also affects the reflection gain for some LoS paths. Therefore, the reflection gain for some device locations is reduced, which limits the minimum probability of detection across the coverage area.

In contrast, J_2 is independent of α , i.e., the phase-shift design considers the LoS paths to the coverage area only. As a result, the LoS and NLoS paths are equally reflected to the AP when the scattering is within the coverage area. Although this approach leads to more variations in the device-RIS channel, we observe in Fig. 6 that it provides the highest minimum probability of detection for $\alpha = 10^\circ$. However, as α increases, the best performance is achieved by J_1 , which explicitly reduces the impact of the scattered paths.

G. Impact of Side Lobes

In order to highlight the difference between objective functions J_1 and J_2 , Fig. 7 illustrates the reflection pattern of the RIS for the phase shifts designed with both J_1 and J_2 , respectively, i.e., it displays the reflection gain $|g(\Psi(q_r), \Psi(q_t))|^2$ for all locations $\{q_t \mid x_{q_t} = -10 \text{ m}, -60 \text{ m} < y_{q_t} < 20 \text{ m}, 0 \text{ m} < z_{q_t} < 60 \text{ m}\}$. As in the schematic view in Fig. 2, the arrows in Fig. 7 indicate the incident directions of the two scattered paths and the rectangle marks the coverage area.

One can see in Fig. 7b that the reflection pattern for J_2 has a wide main lobe that is centered at the coverage area and slowly decays at both sides. In addition, both scattered paths are covered by the side lobes of the reflection pattern, i.e., the channel variations of the device-RIS channel are reflected to the AP. The phase-shift design used in Fig. 7b results in $\min_{q_t \in \mathcal{Q}} P_D(q_t) = 0.95$.

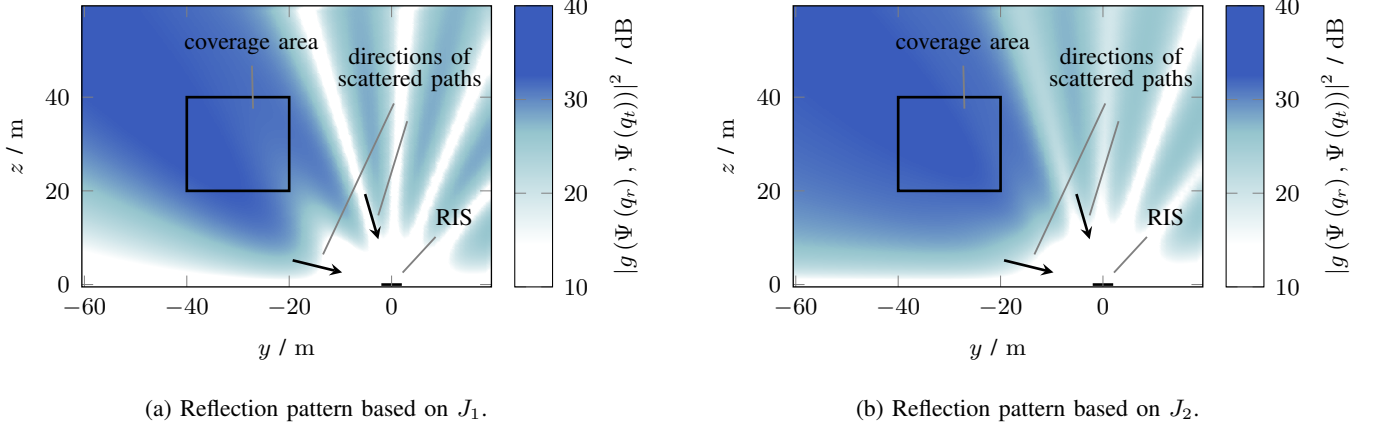


Fig. 7: Reflection patterns for $D_y = 20$ m, $P_{tx} = 0$ dBm, $\alpha = 30^\circ$, and $K = 3$ dB.

In contrast, the reflection pattern for J_1 comprises two narrow main lobes that are directed to the corners of the coverage area. Furthermore, the side lobes affecting the scattered paths in Fig. 7a are significantly reduced compared to those in Fig. 7b. Thus, less variations of the device-RIS channel are reflected to the AP and the detection performance increases to $\min_{q_t \in \mathcal{Q}} P_D(q_t) = 0.99$.

H. Impact of Area Size

As one can observe in Fig. 8, the size of the coverage area is also a limiting factor for the minimum guaranteed probability of detection. As expected, the figure shows that the detection performance decreases with increasing D_y because the reflection gain of the RIS is distributed over a larger area. Moreover, Fig. 8 emphasizes the large gain that the optimized phase-shift designs achieve compared to the baseline quadratic design.

It is worth noting that phase shifts designed based on J_1 and J_2 , respectively, provide almost same the performance for $D_y = 30$ m. In this case, the scatterers are close to the corner of the coverage area, i.e., the impact of the NLoS paths cannot be minimized by J_1 without reducing the reflection gain of the LoS paths.

I. Impact of RIS Size

Finally, we show the impact of the RIS size on the detection performance in Fig. 9. More specifically, we show the minimum probability of detection for different numbers of unit cells $U \in \{32, 48, 64\}$. Fig. 9 indicates that the detection performance improves when the size of the

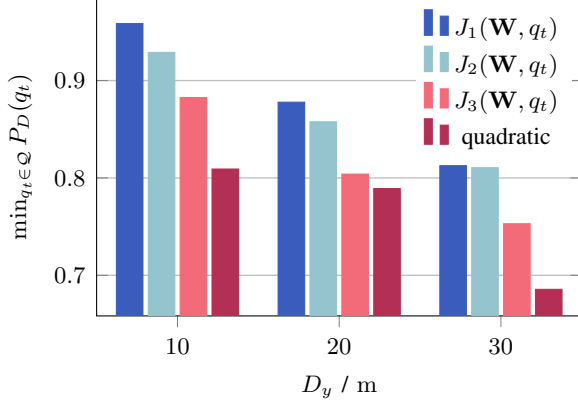


Fig. 8: Minimum probability of detection as a function of area width for $K = 3$ dB, $P_{\text{tx}} = -3$ dBm, and $\alpha = 30^\circ$.

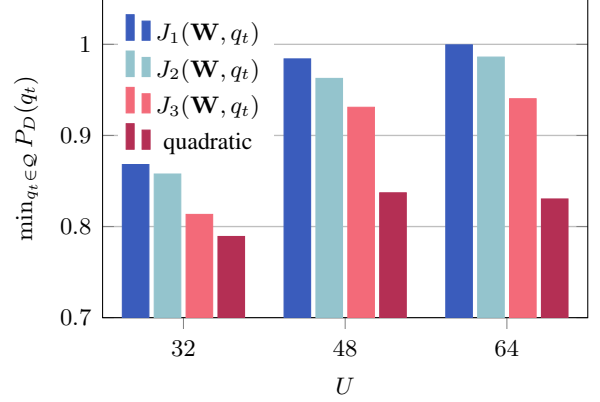


Fig. 9: Minimum probability of detection as a function of RIS cells for $K = 3$ dB, $P_{\text{tx}} = -3$ dBm, $D_y = 20$ m, and $\alpha = 30^\circ$.

RIS increases, which is expected because more signal energy can be reflected to the AP with larger RISs. As U changes from 32 to 64, we observe an improvement of at least 14 % for the optimized phase-shift designs. Moreover, the differences between the design approaches remain the same, i.e., the best performance is achieved with J_1 , followed by J_2 , J_3 , and the baseline quadratic design. The latter does not yield a large gain as U increases because the phase shifts are not specifically designed to maximize the minimum probability of detection. Consequently, the illumination of some parts of the coverage area may not be improved with larger RIS size, which limits the minimum detection performance across the coverage area.

VII. CONCLUSION

This paper studied device activity detection for GF uplink transmission in RIS assisted communication systems, where the RIS was deployed to cover a specific area. In order to optimally design the phase shifts of the RIS, we employed GLRT for device activity detection and showed that the resulting probability of detection can be expressed in terms of the Marcum Q function. Furthermore, we formulated an optimization problem for the RIS phase shifts for maximization of the minimum probability of detection across the coverage area. The non-convexity of the optimization problem was tackled by applying the MM principle and using two approximations of the Marcum Q function. Based on a lower bound of the Marcum Q function, the first approximation resulted in the best detection performance in most cases because all system parameters and the channel statistics are taken into account for phase-shift optimization.

For the second approximation, we neglected the scattered paths of the channel for phase-shift optimization and showed that a similar performance as for the first approximation is achieved when the LoS paths of the channel are dominant or when the NLoS paths and LoS paths of the channel share the same incident angles. In addition, the second approximation resulted in an versatile objective function for phase-shift optimization because it does not depend on system parameters such as transmit power, noise power, and probability of false alarm. Finally, our performance evaluation revealed that maximizing the average channel gain is not a suitable phase-shift design criterion for RIS assisted device activity detection. Although the resulting phase-shift design outperforms the baseline quadratic design, the proposed designs based on approximations of the Marcum Q function yield a significantly higher performance.

REFERENCES

- [1] F. Laue, V. Jamali, and R. Schober, "IRS-assisted active device detection," in *Proc. IEEE 22nd International Workshop on Signal Processing Advances in Wireless Communications (SPAWC)*, Sep. 2021.
- [2] N. Kaina, M. Dupré, G. Lerosey, and M. Fink, "Shaping complex microwave fields in reverberating media with binary tunable metasurfaces," *Scientific Reports*, vol. 4, no. 1, Oct. 2014.
- [3] M. D. Renzo, M. Debbah, D.-T. Phan-Huy, A. Zappone, M.-S. Alouini, C. Yuen, V. Sciancalepore, G. C. Alexandropoulos, J. Hoydis, H. Gacanin, J. de Rosny, A. Bounceur, G. Lerosey, and M. Fink, "Smart radio environments empowered by reconfigurable AI meta-surfaces: an idea whose time has come," *EURASIP Journal on Wireless Communications and Networking*, vol. 2019, no. 1, May 2019.
- [4] L. Dai, B. Wang, M. Wang, X. Yang, J. Tan, S. Bi, S. Xu, F. Yang, Z. Chen, M. D. Renzo, C.-B. Chae, and L. Hanzo, "Reconfigurable intelligent surface-based wireless communications: Antenna design, prototyping, and experimental results," *IEEE Access*, vol. 8, pp. 45 913–45 923, Mar. 2020.
- [5] X. Pei, H. Yin, L. Tan, L. Cao, Z. Li, K. Wang, K. Zhang, and E. Björnson, "Ris-aided wireless communications: Prototyping, adaptive beamforming, and indoor/outdoor field trials," Feb. 2021. [Online]. Available: <https://arxiv.org/abs/2103.00534>
- [6] L. You, J. Xiong, D. W. K. Ng, C. Yuen, W. Wang, and X. Gao, "Energy efficiency and spectral efficiency tradeoff in RIS-aided multiuser MIMO uplink transmission," *IEEE Trans. Signal Process.*, vol. 69, pp. 1407–1421, Dec. 2021.
- [7] L. Wei, C. Huang, G. C. Alexandropoulos, C. Yuen, Z. Zhang, and M. Debbah, "Channel estimation for RIS-empowered multi-user MISO wireless communications," *IEEE Trans. Commun.*, vol. 69, no. 6, pp. 4144–4157, Jun. 2021.
- [8] Y. Liu, J. Zhao, M. Li, and Q. Wu, "Intelligent reflecting surface aided MISO uplink communication network: Feasibility and power minimization for perfect and imperfect CSI," *IEEE Trans. Commun.*, vol. 69, no. 3, pp. 1975–1989, Mar. 2021.
- [9] S. Luo, P. Yang, Y. Che, K. Yang, K. Wu, K. C. Teh, and S. Li, "Spatial modulation for RIS-assisted uplink communication: Joint power allocation and passive beamforming design," *IEEE Trans. Commun.*, vol. 69, no. 10, pp. 7017–7031, Oct. 2021.
- [10] K. Zhi, C. Pan, H. Ren, and K. Wang, "Uplink achievable rate of intelligent reflecting surface-aided millimeter-wave communications with low-resolution ADC and phase noise," *IEEE Wireless Communications Letters*, vol. 10, no. 3, pp. 654–658, Mar. 2021.

- [11] Y. Xu, Z. Gao, Z. Wang, C. Huang, Z. Yang, and C. Yuen, "RIS-enhanced WPCNs: Joint radio resource allocation and passive beamforming optimization," *IEEE Trans. Veh. Technol.*, vol. 70, no. 8, pp. 7980–7991, Aug. 2021.
- [12] L. You, J. Xiong, Y. Huang, D. W. K. Ng, C. Pan, W. Wang, and X. Gao, "Reconfigurable intelligent surfaces-assisted multiuser MIMO uplink transmission with partial CSI," *IEEE Trans. Wireless Commun.*, vol. 20, no. 9, pp. 5613–5627, Sep. 2021.
- [13] L. Liu and W. Yu, "Massive connectivity with massive MIMO – part I: Device activity detection and channel estimation," *IEEE Trans. Signal Process.*, vol. 66, no. 11, pp. 2933–2946, Jun. 2018.
- [14] T. Ding, X. Yuan, and S. C. Liew, "Sparsity learning-based multiuser detection in grant-free massive-device multiple access," *IEEE Trans. Wireless Commun.*, vol. 18, no. 7, pp. 3569–3582, Jul. 2019.
- [15] X. Shao, X. Chen, and R. Jia, "A dimension reduction-based joint activity detection and channel estimation algorithm for massive access," *IEEE Trans. Signal Process.*, vol. 68, pp. 420–435, Jan. 2020.
- [16] X. Zhang, F. Labeau, L. Hao, and J. Liu, "Joint active user detection and channel estimation via Bayesian learning approaches in MTC communications," *IEEE Trans. Veh. Technol.*, vol. 70, no. 6, pp. 6222–6226, Jun. 2021.
- [17] D. Jiang and Y. Cui, "ML and MAP device activity detections for grant-free massive access in multi-cell networks," *IEEE Trans. Wireless Commun.*, 2021, early access.
- [18] M. Guo and M. C. Gursoy, "Sparse activity detection in intelligent reflecting surface assisted wireless networks," in *Proc. IEEE 32nd Annual International Symposium on Personal, Indoor and Mobile Radio Communications (PIMRC)*, Sep. 2021.
- [19] S. Xia, Y. Shi, Y. Zhou, and X. Yuan, "Reconfigurable intelligent surface for massive connectivity: Joint activity detection and channel estimation," *IEEE Trans. Signal Process.*, vol. 69, pp. 5693–5707, Oct. 2021.
- [20] X. Shao, L. Cheng, X. Chen, C. Huang, and D. W. K. Ng, "A Bayesian tensor approach to enable RIS for 6G massive unsourced random access," in *Proc. IEEE Global Communications Conference (GLOBECOM)*, Dec. 2021.
- [21] M. Najafi, V. Jamali, R. Schober, and H. V. Poor, "Physics-based modeling and scalable optimization of large intelligent reflecting surfaces," *IEEE Trans. Commun.*, vol. 69, no. 4, pp. 2673–2691, Dec. 2020.
- [22] V. Popov, M. Odit, J.-B. Gros, V. Lenets, A. Kumagai, M. Fink, K. Enomoto, and G. Lerosey, "Experimental demonstration of a mmWave passive access point extender based on a binary reconfigurable intelligent surface," Jul. 2021. [Online]. Available: <https://arxiv.org/abs/2107.02087>
- [23] V. Croisfelt, F. Saggese, I. Leyva-Mayorga, R. Kotaba, G. Gradoni, and P. Popovski, "A random access protocol for RIS-aided wireless communications," 2022. [Online]. Available: <https://arxiv.org/abs/2203.03377>
- [24] H. Shen, W. Xu, S. Gong, C. Zhao, and D. W. K. Ng, "Beamforming optimization for IRS-aided communications with transceiver hardware impairments," *IEEE Trans. Commun.*, vol. 69, no. 2, pp. 1214–1227, Feb. 2021.
- [25] Z. Xing, R. Wang, J. Wu, and E. Liu, "Achievable rate analysis and phase shift optimization on intelligent reflecting surface with hardware impairments," *IEEE Trans. Wireless Commun.*, vol. 20, no. 9, pp. 5514–5530, Sep. 2021.
- [26] Z. Xing, R. Wang, X. Yuan, and J. Wu, "Location-aware beamforming design for reconfigurable intelligent surface aided communication system," in *Proc. IEEE/CIC International Conference on Communications in China (ICCC)*, Jul. 2021.
- [27] V. Jamali, M. Najafi, R. Schober, and H. V. Poor, "Power efficiency, overhead, and complexity tradeoff of IRS codebook design - quadratic phase-shift profile," *IEEE Commun. Lett.*, vol. 25, no. 6, pp. 2048–2052, Jun. 2021.
- [28] Q. Wu and R. Zhang, "Intelligent reflecting surface enhanced wireless network: Joint active and passive beamforming design," in *Proc. IEEE Global Communications Conference (GLOBECOM)*, Dec. 2018.
- [29] —, "Towards smart and reconfigurable environment: Intelligent reflecting surface aided wireless network," *IEEE Communications Magazine*, vol. 58, no. 1, pp. 106–112, Jan. 2020.
- [30] Z. Wang, L. Tan, H. Yin, K. Wang, X. Pei, and D. Gesbert, "A received power model for reconfigurable intelligent

- surface and measurement-based validations,” in *Proc. IEEE 22nd International Workshop on Signal Processing Advances in Wireless Communications (SPAWC)*, Sep. 2021.
- [31] X. Rao and V. K. N. Lau, “Distributed compressive CSIT estimation and feedback for FDD multi-user massive MIMO systems,” *IEEE Trans. Signal Process.*, vol. 62, no. 12, pp. 3261–3271, Jun. 2014.
 - [32] K. Zhi, C. Pan, H. Ren, K. Wang, and M. Elkashlan, “Reconfigurable intelligent surface-aided MISO systems with statistical CSI: Channel estimation, analysis and optimization,” in *Proc. IEEE 22nd International Workshop on Signal Processing Advances in Wireless Communications (SPAWC)*, Sep. 2021.
 - [33] G. Yu, X. Chen, C. Zhong, D. W. K. Ng, and Z. Zhang, “Design, analysis, and optimization of a large intelligent reflecting surface-aided b5g cellular internet of things,” *IEEE Internet of Things Journal*, vol. 7, no. 9, pp. 8902–8916, Sep. 2020.
 - [34] D. Xu, X. Yu, Y. Sun, D. W. K. Ng, and R. Schober, “Resource allocation for IRS-assisted full-duplex cognitive radio systems,” *IEEE Trans. Commun.*, vol. 68, no. 12, pp. 7376–7394, Dec. 2020.
 - [35] Y. Wang, Y. Zhang, Z. Tian, G. Leus, and G. Zhang, “Super-resolution channel estimation for arbitrary arrays in hybrid millimeter-wave massive MIMO systems,” *IEEE Journal of Selected Topics in Signal Processing*, vol. 13, no. 5, pp. 947–960, Sep. 2019.
 - [36] S. M. Kay, *Fundamentals of Statistical Signal Processing, Volume II: Detection Theory*. Prentice Hall, 1998.
 - [37] —, *Fundamentals of Statistical Processing, Volume I*. Prentice Hall, 1993.
 - [38] J. Proakis, *Digital Communications*. McGraw-Hill, 2008.
 - [39] V. M. Kapinas, S. K. Mihos, and G. K. Karagiannidis, “On the monotonicity of the generalized marcum and nuttall Q-functions,” *IEEE Trans. Inf. Theory*, vol. 55, no. 8, pp. 3701–3710, Aug. 2009.
 - [40] Y. Sun, Á. Baricz, and S. Zhou, “On the monotonicity, log-concavity, and tight bounds of the generalized marcum and nuttall Q-functions,” *IEEE Trans. Inf. Theory*, vol. 56, no. 3, pp. 1166–1186, Mar. 2010.
 - [41] Á. Baricz and Y. Sun, “New bounds for the generalized marcum Q-function,” *IEEE Trans. Inf. Theory*, vol. 55, no. 7, pp. 3091–3100, Jul. 2009.
 - [42] A. Annamalai, “New exponential-type integral representations of the generalized marcum Q-function of real-order with applications,” in *Proc. IEEE 12th Malaysia International Conference on Communications (MICC)*, Nov. 2015.
 - [43] A. Annamalai and C. Tellambura, “A simple exponential integral representation of the generalized marcum Q-function for real-order m with applications,” in *Proc. IEEE Military Communications Conference (MILCOM)*, Nov. 2008.
 - [44] X. Yu, D. Xu, Y. Sun, D. W. K. Ng, and R. Schober, “Robust and secure wireless communications via intelligent reflecting surfaces,” *IEEE J. Sel. Areas Commun.*, vol. 38, no. 11, pp. 2637–2652, Nov. 2020.
 - [45] Y. Sun, P. Babu, and D. P. Palomar, “Majorization-minimization algorithms in signal processing, communications, and machine learning,” *IEEE Trans. Signal Process.*, vol. 65, no. 3, pp. 794–816, Feb. 2017.
 - [46] S. Boyd and L. Vandenberghe, *Convex Optimization*. Cambridge University Press, 2004.
 - [47] K. Yang, T. Jiang, Y. Shi, and Z. Ding, “Federated learning based on over-the-air computation,” in *Proc. IEEE International Conference on Communications (ICC)*, May 2019.
 - [48] Z. Luo, W. Ma, A. So, Y. Ye, and S. Zhang, “Semidefinite relaxation of quadratic optimization problems,” *IEEE Signal Process. Mag.*, vol. 27, no. 3, pp. 20–34, May 2010.
 - [49] H. Liu, X. Yuan, and Y.-J. A. Zhang, “Matrix-calibration-based cascaded channel estimation for reconfigurable intelligent surface assisted multiuser MIMO,” *IEEE J. Sel. Areas Commun.*, vol. 38, no. 11, pp. 2621–2636, Nov. 2020.
 - [50] P. Mursia, V. Sciancalepore, A. Garcia-Saavedra, L. Cottatellucci, X. C. Perez, and D. Gesbert, “RISMA: Reconfigurable intelligent surfaces enabling beamforming for IoT massive access,” *IEEE J. Sel. Areas Commun.*, vol. 39, no. 4, pp. 1072–1085, Apr. 2021.